Applied Catalysis B: Environmental 334 (2023) 122792

Contents lists available at ScienceDirect

Applied Catalysis B: Environmental

journal homepage: www.elsevier.com/locate/apcatb

Controlled electron transfer at the Ni-ZnO interface for ultra-fast and stable hydrogenation of N-propylcarbazole

Yinheng Zhao [a], Chenggen Li [a,b], Yuanzheng Zhu [a], Li Liu [a], Ting Zhu [a], Yuan Dong [a], Hansong Cheng [a], Ming Yang [a,b,*]

[a] Hubei Hydrogen Energy Technology Innovation Center, Faculty of Materials Science and Chemistry, China University of Geosciences, Wuhan 430074, PR China
[b] Key Laboratory of Geological Survey and Evaluation of Ministry of Education, Institute of Advanced Studies, China University of Geosciences, Wuhan 430074, PR China

ARTICLE INFO

Keywords:
Liquid organic hydrogen carriers
ZnO-modified Ni catalysts
Controlled electron transfer
Ni-ZnO interface
Catalytic hydrogenation

ABSTRACT

Developing cost-effective and efficient hydrogenation catalysts is crucial for Liquid Organic Hydrogen Carrier (LOHC) technology. ZnO-modified Ni/Al_2O_3 catalysts were prepared and evaluated for their catalytic hydrogenation of N-propylcarbazole (NPCZ). Among all catalysts, $NiZn_{11}Al$ achieved saturation hydrogenation of NPCZ within 25 min and exhibited excellent potential for industrial applications. The moderate amount of ZnO enhanced the dispersion of Ni nanoparticles, while excessive ZnO inhibited dispersion and promoted Ni-Zn alloy formation. The amount of ZnO doping determined the interaction strength and direction of electron transfer between Ni and ZnO. The formation of the Ni-ZnO interface effectively prevented agglomeration of Ni nanoparticles and improved catalytic stability for NPCZ hydrogenation. Dispersed $Ni^{\delta+}$ boosted hydrogen activation, and the strong acid sites of the catalyst promoted the hydrogenation activity. The synergistic effect of Ni and ZnO was shown to accelerate the hydrogenation rate and lower the activation energy compared with Ru-based catalysts.

1. Introduction

Hydrogen has emerged as a sustainable and environmentally friendly energy source owing to its high energy density and zero carbon emissions [1–4]. Replacing fossil fuels with hydrogen is a promising strategy for achieving "carbon peaking and carbon neutralization" [5,6]. Nonetheless, the safe and efficient storage and transportation of hydrogen remains a major hurdle to its large-scale deployment, given its highly flammable and explosive nature. Liquid Organic Hydrogen Carriers (LOHCs) have been proposed as an efficient method for utilizing hydrogen through reversible hydrogenation and dehydrogenation of liquid hydrocarbons [7–9], enabling storage and transportation under mild conditions [10–12]. For instance, Chiyoda has reported that the toluene-methylcyclohexane system is highly efficient for long-distance transportation and successive utilization of overseas hydrogen. Similarly, Hydrogenious Technologies is building the world's largest LOHCs plant based on dibenzyltoluene (DBT). However, the harsh dehydrogenation conditions faced by traditional aromatic LOHCs is a major challenge [13,14]. To address this challenge, heteroatoms (N, O, S, etc.) have been introduced into the aromatic ring of LOHCs to reduce the dehydrogenation enthalpy of the hydrogen storage molecule [15–17]. A variety of novel heterocycle LOHCs molecules, such as indoles [18], quinolines [19], and carbazoles [20,21], have been reported for reversible storage and release of hydrogen. Among these heterocycles, dodecahydro-N-propylcarbazole (12H-NPCZ) is noteworthy due to its low melting point, liquid state at room temperature, and compatibility with existing oil transportation pipeline facilities.

Efficient and cost-effective catalysts are crucial for the widespread adoption of LOHCs. The synergistic effects between different components in heterogeneous catalysts has a positive impact on reducing reaction activation energy of hydrogenation and increasing the catalytic reaction rate. Ge et al. [22] found that Beta zeolite in Ru/BEA catalysts could effectively accept and transfer H* radicals generated by $Ru^{\delta+}$ activated H_2, promoting hydrogen spillover, which exhibited excellent activity in the hydrogenation of N-Ethylcarbazole (NECZ) with the hydrogen uptake of 5.69 wt% within 1.5 h for the 6 MPa H_2 at 100 °C.

* Corresponding author at: Hubei Hydrogen Energy Technology Innovation Center, Faculty of Materials Science and Chemistry, China University of Geosciences, Wuhan 430074, PR China.
E-mail address: yangming8180@gmail.com (M. Yang).

https://doi.org/10.1016/j.apcatb.2023.122792
Received 18 March 2023; Received in revised form 13 April 2023; Accepted 19 April 2023
Available online 20 April 2023
0926-3373/© 2023 Elsevier B.V. All rights reserved.

Xue et al. [23] found that the introduction of Co atoms in the Rh/γ-Al_2O_3 catalyst made the d band center of Rh atom move to Fermi level, which improved the reaction energy and promoted the reaction kinetics. Rh_1Co/γ-Al_2O_3 catalyst showed excellent catalytic activity for (de)hydrogenation of NECZ, a low temperature of 90 °C was realized for the complete hydrogenation (100%). Yu et al. [21] found that $LaNi_5$ nanoparticles with surface Pd deposited exhibited better activity than Pd/Al_2O_3 for (de)hydrogenation of NECZ. Excellent catalytic activity was attributed to ample lattice H bonding sites and fast H diffusion kinetics in $LaNi_5$ nanoparticles. Meanwhile the formation of Pd/$LaNi_5$ interface facilitated the transfer of hydrogen species between $LaNi_5$ and organic molecules adsorbed on Pd. The precious metals represented by Rh and Pd have a high price. As a result, researchers are gradually turning their attention to non-precious metal hydrogenation catalysts with low prices. Ni-based catalysts are a suitable alternative for N-heterocycle hydrogenation due to their abundance and affordability [24]. However, the activity and stability of Ni-based catalysts have much room for improvement [25,26]. A study by our group [27] demonstrated that a high-loading Ni/Al_2O_3-SiO_2 catalyst prepared by co-precipitation could achieve saturated hydrogenation of NPCZ at 150 °C and 7 MPa H_2 in 60 min, with the increased activity attributed to the weakening interaction between Ni and Al_2O_3-SiO_2. However, the activity of Ni/Al_2O_3-SiO_2 decreased significantly after 5 cycles due to the aggregation of Ni nanoparticles. Adding promoters to catalysts to synergize with Ni is a potential solution for improving catalytic performance. Liu et al. [28] reported that Ni-Rh bimetallic catalysts exhibited a high yield of 12H-NECZ within 2 h under 150 °C and 7 MPa H_2 pressure, which was attributed to the introduction of Rh atoms increased the reduction and dispersion of Ni species Similarly, Wu and Li et al. [29] prepared YH_3-doped Ni/Al_2O_3 by high-energy ball milling, revealing excellent NECZ hydrogenation activity comparable to the best Ru/Al_2O_3 catalyst, with an enhancement mechanism ascribed to the new pathway for the transfer of hydrogen species via YH_3. Although these additives have significantly improved catalytic performance, their high cost, complicated preparation process, and instability have limited their industrial application. Hence, there is a growing demand to explore low-cost and efficient promoters.

ZnO is widely adopted in C1 chemistry and photocatalysis due to its favorable chemical stability, excellent sulfur resistance, and low cost. Wang et al. [30] demonstrated that Ni-ZnO/SiO_2 exhibited excellent catalytic activity in the preparation of formic acid by hydrogenation of $NaHCO_3$, with 97.0% formic acid yield in 2 h of reaction at 260 °C and 3 MPa hydrogen pressure. Similarly, Murthy et al. [31] investigated the effect of ZnO on CO_2 hydrogenation over Ni/MCM-41 catalyst and reported that the selectivity of CO increased from 85.9% to 96.2% at 600 °C when the Zn loading was reduced from 7.5% to 1%. Wu et al. [32] discovered that Ni/C exhibited significant deactivation during catalytic styrene hydrogenation with a deactivation rate of 42.16% after seven catalytic reactions, and the stability of the catalyst was significantly enhanced by doping with ZnO, reducing the deactivation rate of Ni-ZnO/C to 3.02%. Overall, ZnO-modified Ni-based catalysts have been widely employed in various chemical systems. However, their application in LOHCs remains understudied.

In the present study, ZnO-modified Ni-based catalysts were developed using the co-precipitation method, which were employed for N-heterocyclic hydrogenation for the first time. We investigated the effect of ZnO doping amount on the catalyst structure and catalytic performance, based on 50 wt% loading of Ni. Our findings showed that a moderate amount of ZnO could improve the pore structure and surface electron modification of Ni-based catalysts, thereby enhancing the hydrogenation activity of NPCZ. By combining DFT theoretical calculations and a series of characterization results, we have revealed the promotion mechanism of Ni-Zn structural features on the hydrogenation of NPCZ.

2. Experimental

2.1. Catalyst preparation

The preparation of the catalysts was carried out using an established co-precipitation method. All chemicals, including Hexane (AR, 99.5%), $Ni(NO_3)_2{\cdot}6\,H_2O$ (AR), $Al(NO_3)_3{\cdot}9\,H_2O$ (AR), $Zn(NO_3)_2{\cdot}6\,H_2O$ (AR), Na_2CO_3 and PEG 2000 (AR) were purchased from Sinopharm Chemical Reagent Co. Ltd. Argon-hydrogen mixed gas (10 vol% H_2), argon-oxygen mixed gas (1 vol% O_2) and high-purity hydrogen (99.999%) were supplied by Wuhan Run Huahui Oxygen Cylinder Inspection Co. Ltd. N-propylcarbazole (NPCZ) was supplied by Hechang Chemical Co. Ltd. All chemicals were used for the synthesis of the catalysts without further purification.

In the first step of the preparation process, a solution (Solution A) consisting of $Ni(NO_3)_2{\cdot}6\,H_2O$, $Al(NO_3)_3{\cdot}9\,H_2O$, and $Zn(NO_3)_2{\cdot}6\,H_2O$ was dissolved in 100 mL of ultrapure water. In a separate solution (Solution B), a certain amount of Na_2CO_3 was dissolved in 100 mL of ultrapure water. A mixture of 0.5 g PEG 2000 and 200 mL ultrapure water was named Solution C. Solutions A and B were added dropwise to solution C under vigorous stirring. The mixture was then aged at 90 °C for 2 h. The blue-green precipitate obtained was washed several times with ultrapure water and dried at 100 °C for 12 h.

The dried materials were calcined in an air atmosphere at 600 °C for 1 h and reduced by 10% H_2/Ar at 650 °C for 3 h. The samples were passivated with 1% O_2/Ar before being removed. The final prepared catalysts were denoted as $NiZn_xAl$(x represents the mass load of Zn). NiAl and NiZn represent Ni loaded on pure Al_2O_3 and pure ZnO respectively. The theoretical loading of Ni for all the catalysts in this work was 50 wt%.

2.2. Catalyst characterization

To analyze the physical properties of the catalysts, several characterization techniques were employed. Nitrogen isothermal sorption (N_2 adsorption–desorption) was carried out on the ASAP 2020 physical adsorption instrument. The crystal phase structure of the catalyst samples was analyzed using a Bruker AXS model D8-Focus X-ray diffractometer (XRD, Bruker AXS, Cu-Ka-ray), Germany. Transmission electron microscopy (TEM) with high-resolution transmission electron microscope (FEI TF20, energy spectrum model Super-X) was used to observe the supported Ni nanoparticles. H_2 temperature-programmed reduction (H_2-TPR), NH_3 temperature-programmed desorption (NH_3-TPD), and H_2 temperature-programmed desorption (H_2-TPD) were performed on a Micromeritics AutoChem 2950 II instrument to further characterize the catalysts. The actual elemental content of Ni, Al, and Zn were measured by the OPTIMA 5300 DV Inductively Coupled Plasma Emission Spectrometer (ICPOES, OPTIMA5300DV) from PerkinElmer, USA.

2.3. Hydrogenation of NPCZ

The catalytic performance of catalysts was performed in a 250 mL autoclave batch reactor (Shanghai LABE instrument LB250). A mixture of 0.2 g catalyst, 2 g NPCZ, and 40 mL n-hexane was added to the reactor. The hydrogenation reaction was carried out at 150 °C, 7 MPa, and 600 r/min. During the process, a small amount of liquid sample was removed from the reaction system at regular intervals. The composition of the liquid mixture was analyzed by GC (Agilent GC 7890B).

The experimental details of the catalyst stability test are as follows: After the catalytic reaction was completed and the reactor cooled to room temperature, the catalyst was settled naturally. We aspirated the supernatant carefully by using a rubber tipped dropper, and washed the catalyst several times with n-hexane. The supernatant obtained by washing the catalyst was tested using GC. The next hydrogenation cycle was carried out when confirming that 12H-NPCZ was not present in the supernatant. All experiments were performed at 150 °C and 7 MPa

hydrogen pressure. The fresh catalyst and the recovered catalyst after cycling experiments were denoted as $NiZn_xAl$-F and $NiZn_xAl$-C, respectively.

2.4. Computational method

The catalyst was evaluated using a Density Functional Theory (DFT) theoretical level with the Vienne Ab Initio Simulation Package, using plane waves to describe the Kohn-Sham single-electron state [33,34]. The calculations were carried out using a Perdew-Burke-Ernzerhof (PBE) exchange-correlation function in the form of a generalized gradient approximation (GGA) [35]. The ion cores of all atoms were described using the projector-enhanced wave method (PAW) with a cut-off energy of 400 eV [36]. A Gamma method with a smearing of 0.2 eV was carried out, and the Brillouin-zone integration was restricted to 1 × 1 × 1 k-point.

The three-fold ZnO slab contains 144 atoms, while the lattice parameters of the ZnO(100) surface are a = 14.26 Å, b = 14.26 Å, and c = 24.56 Å. The thickness of the ZnO(100) slab is about 6 Å with a vacuum layer of 18 Å in the Z-direction to avoid periodic structural interactions. The slab model consists of six layers of atoms, where the bottom three layers are fixed, while the remaining three layers are relaxed. Spin polarization is used in all computational models. The energy convergence criterion for structure optimization is 1×10^{-5} eV/atom, while the convergence criterion for force is 0.02 eV/Å.

3. Results and discussion

3.1. Characterization

3.1.1. Structural properties characterization

Table 1 and Table S1 present the specific surface area, pore volume, and pore size data for all the catalysts studied. The N_2 physical adsorption-desorption isotherms for all catalysts in Fig. 1a and Fig. S1a, c exhibit type-IV curves, characteristic of mesoporous structures. The hysteresis loops observed at high pressure (P/P_0 =0.66–0.98) provide evidence of the existence of large mesopores [37]. The NiAl catalyst has a specific surface area of 180 m^2/g and a pore volume of 0.54 cm^3 /g. Upon introducing a small amount of ZnO into NiAl, the specific surface area of the $NiZn_6Al$ catalyst increased to 218.47 m^2/g, and its pore volume improved to 0.75 cm^3/g. The increase in the specific surface area and pore volume of the $NiZn_6Al$ catalyst could be attributed to the migration of ZnO from the sub-surface to the surface, resulting in more internal voids and an increased specific surface of the catalysts [38,39]. This phenomenon was consistent with the findings of Wong et al. [40]. However, upon increasing the ZnO content beyond a certain level, the specific surface area and pore capacity of catalysts gradually decrease and the average pore size increased, with the NiZn catalyst showed almost no specific surface area. It might be related to the characteristics of ZnO, which is typically known to possess only a small amount of large mesopores, or no pores at all. It is noteworthy that the $NiZn_{18}Al$ catalyst has a larger pore capacity of 0.72 cm^3/g, which was probably due to the high doping of ZnO in $NiZn_{18}Al$ catalyst, leading to produce more large-sized stacked holes and increase the pore volume. The mesopore size distribution curves for $NiZn_xAl$ catalysts, derived by Barrett-Joyner-Halenda (BJH), are shown in Fig. 1b. All catalysts exhibit a bimodal distribution, with peaks centered at 3 nm and 9 nm, respectively. The intensity of the pore size distribution peaks diminishes significantly with increasing ZnO content, and the center of the peak at 9 nm gradually shifts towards larger pore sizes.

The XRD characterization of catalysts is shown in Fig. 1c and Fig. S1e. The Ni particle size was calculated using the Scherrer equation and the results are presented in Table S1. The NiAl catalyst exhibited diffraction peaks at 44.5°, 51.9°, and 76.4°, which were attributed to Ni (PDF#87–0712). In addition, the diffraction peaks at 31.5°, 37.0°, 59.7°, and 65.5° were assigned to the $NiAl_2O_4$ spinel structure (PDF#10–0339). It was observed that the intensity of the diffraction peaks of $NiAl_2O_4$ and Ni nanoparticles decreased as the Zn content increased. In particular, the Ni diffraction peak in the $NiZn_{11}Al$ catalyst was the weakest among all catalysts, indicating that the introduction of a small amount of ZnO inhibited the formation of $NiAl_2O_4$ and promoted the dispersion of Ni nanoparticles. As shown in Fig. 1c, the intensity of the Ni diffraction peaks gradually increases when the Zn loading exceeds 1 wt%, indicating that excessive ZnO doping leads to agglomeration of the Ni nanoparticles. It is noteworthy that when the ZnO loading exceeds 18 wt% (Fig. S1e), the Ni diffraction peaks gradually shift towards the low-angle region, with the Ni diffraction peaks in NiZn catalyst shifting to 43.7°, 50.9° and 74.8° respectively, which is attributed to a small amount of Zn atoms entering the Ni lattice, as reported by Meng et al. [41] and Xiao et al. [42]. Furthermore, a series of new diffraction peaks were observed at 31.7°, 34.4°, 36.2°, 46.7°, 56.5° and 62.8°, and further increased in the $NiZn_{35}Al$ catalyst. Of these, the diffraction peak at 46.7° is attributed to a large number of Ni-Zn alloy nanoparticles formed in the catalyst due to high ZnO doping, which species was also found in the study by Wang et al. [43], and the remaining new diffraction peaks are attributed to ZnO nanoparticles. The changes in nanoparticle structure from $NiZn_{11}Al$ to NiZn catalyst demonstrate that excess Zn content leads to the aggregation of Ni nanoparticles and the formation of Ni-Zn alloy, which can negatively impact the catalyst's specific surface area as shown in Table S1.

H_2-TPR analysis was conducted to provide insights into the metal-support interactions in the catalysts. Fig. 1d and Fig. S1f illustrate the H_2-TPR curves of all $NiZn_xAl$ catalysts. The NiAl catalyst exhibited three major broad peaks, as shown in Fig. 1d. The low-temperature reduction peak at 148 °C was assigned to small free NiO nanoparticles. The H_2-consumption peak at 325 °C was attributed to NiO species with strong interaction with the carrier. Upon the addition of ZnO, both H_2-consumption peaks shifted towards the high-temperature region. Specifically, in the $NiZn_{11}Al$ catalyst, the highest reduction temperature increased to 258 °C and 401 °C, respectively. However, with a ZnO loading exceeding 18 wt%, the centers of these two reduction peaks started to move to lower temperatures, dropping to 178 °C and 289 °C in the NiZn catalyst, indicating that the strong metal-support interaction in the $NiZn_{11}Al$ catalyst promotes the dispersion of Ni [44]. The high-temperature peak observed at 703 °C in the NiAl catalyst is due to $NiAl_2O_4$ formed during the preparation process, as observed in XRD. Notably, the introduction of ZnO led to the disappearance of the reduction peak at 703 °C, implying the reduction of $NiAl_2O_4$ in the

Table 1
Physicochemical properties of $NiZn_xAl$ catalysts.

Sample	BET Surface Area (m^2/g)	Pore Volume (cm^3/g)[a]	Average Pore Size (nm)[a]	Loading of Ni (wt%)[b]	Loading of Zn (wt%)[b]	Loading of Al (wt%)[b]
NiZn	—	—	—	40.42	47.87	0
$NiZn_{18}Al$	119	0.72	18.8	37.54	19.89	13.86
$NiZn_{11}Al$	155	0.68	13.3	41.82	12.43	17.76
$NiZn_6Al$	218	0.75	10.8	39.14	6.56	19.58
NiAl	180	0.54	9.6	39.27	0	21.04

a Pore volume and average pore size were calculated according to the BJH method.
b Determined by ICP-OES measurement.

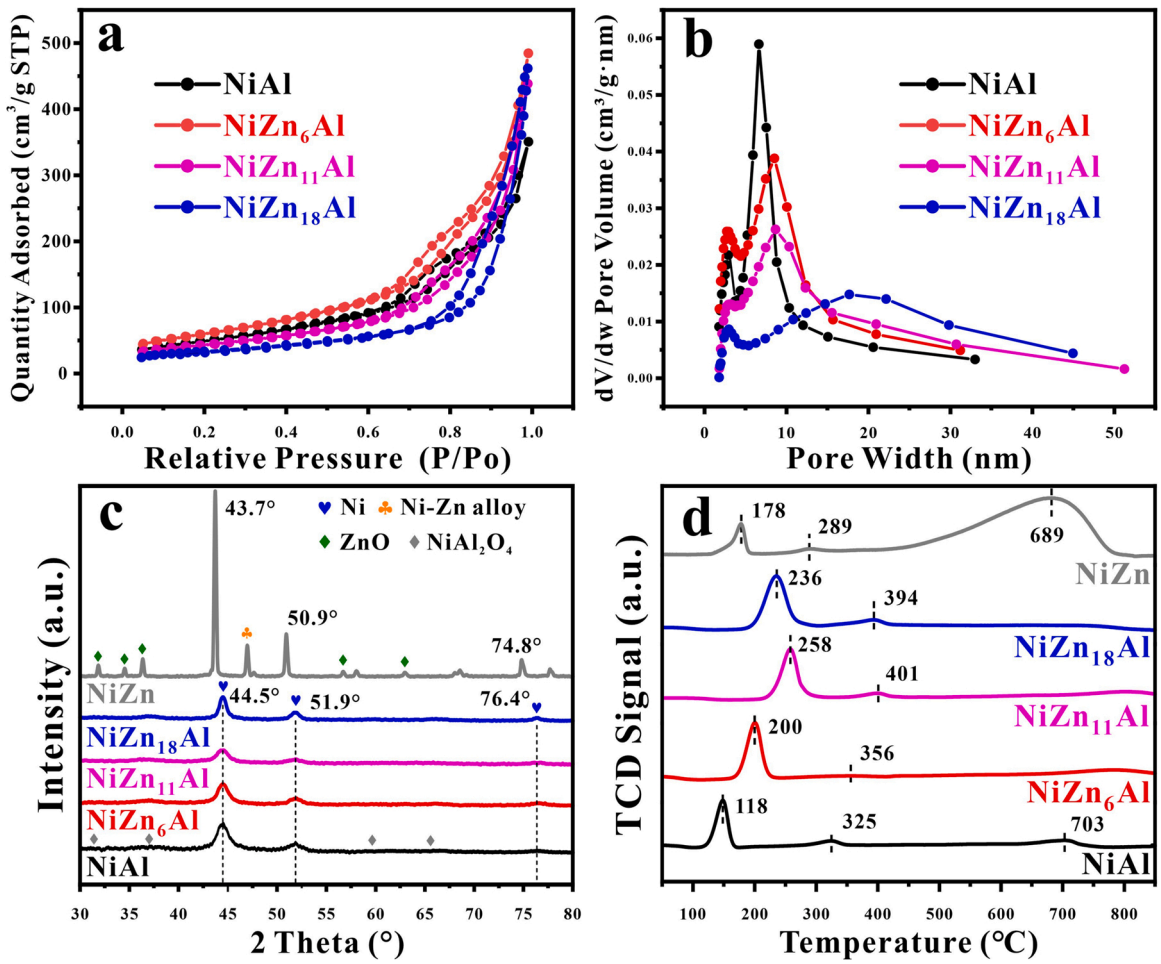

Fig. 1. (a) N_2 physical adsorption-desorption isotherms, (b) pore size distribution, (c) XRD patterns, (d) H_2-TPR curves of $NiZn_xAl$ catalysts.

catalysts. However, when the ZnO loading is 35 wt%, the reduction peak in the high-temperature region is observed again and increases further prominent in the NiZn catalyst (Fig. S2f). Combined with the XRD results, the peaks at 689 °C in $NiZn_{35}Al$ and NiZn catalyst are attributed to the Ni-Zn alloy.

3.1.2. Electron transfer characterization

To investigate the effect of ZnO on catalytic activity, NH_3 and H_2 were used as molecular probes to study the surface acidity of catalysts, as well as the adsorption-desorption properties of hydrogen species.

Fig. 2a shows the desorption peaks centered at 65–150 °C, 250–350 °C, 350–450 °C, and 450–650 °C, which were attributed to weak acid sites, intermediate acid sites, strong acid sites, and ultra-strong acid sites, respectively [45]. Table 2 shows the detailed acid contents of the catalysts. The presence of a large amount of Lewis acid Al^{3+} in the NiAl catalyst resulted in a strong adsorption capacity for NH_3, making its total acid content as high as 583 μmol·g^{-1}, mainly concentrated in the strongly acidic region [46–48]. With the addition of ZnO, the total acid amount of the $NiZn_{11}Al$ catalyst increased significantly, reaching a maximum value of 709 μmol·g^{-1}. This increase was mainly attributed to the increase of medium and strong acid sites, probably related to the interaction between Ni and ZnO. Upon the introduction of excess ZnO, the total acid amount of the $NiZn_{18}Al$ catalyst decreased to 596 μmol·g^{-1}. The acid amount of the NiZn catalyst was only 74 μmol·g^{-1}, which may be due to the low specific surface area of the catalyst. It is noteworthy that the $NiZn_6Al$ catalyst gave a relatively low total acid amount (551 μmol·g^{-1}) compared to NiAl, which was probably due to the weaker interaction between Ni and ZnO being insufficient to compensate for the decreasing total acid amount due to the reduced Al^{3+} content, while ZnO also contains basic sites. The above-described evolution of acid amounts suggests that the loading of ZnO significantly influences the surface acid properties of catalysts, potentially affecting the catalytic performance of the active site [49]. Therefore, it is important to carefully control the amount of ZnO in the catalyst to achieve optimal catalytic activity.

The ability of catalysts to adsorb, dissociate, and desorb hydrogen species can significantly impact hydrogenation reactions [50]. Fig. 2b shows the H_2-TPD curves of catalysts with different ZnO contents. Two types of hydrogen desorption peaks were observed: peaks below 100 °C were assigned to weakly adsorbed hydrogen, while those in the 160–190 °C region were assigned to strongly adsorbed hydrogen species. After the introduction of ZnO, the peak of strongly adsorbed hydrogen gradually shifted toward higher temperatures. The temperature of hydrogen desorption in this catalyst was up to 186 °C due to the stability of the adsorbed hydrogen species in the $NiZn_{11}Al$ catalyst. With the addition of excess ZnO, the center of the high-temperature desorption peak dropped to 163 °C in the $NiZn_{18}Al$ catalyst. No significant effect of ZnO content was observed on weakly adsorbed hydrogen species in the catalysts. It is noteworthy that no hydrogen desorption peaks were observed in the NiZn catalyst, indicating a weak adsorption capacity for hydrogen. The above phenomena demonstrate that a moderate amount of ZnO doping will benefit the stability of the hydrogen species on the catalyst surface. Therefore, ZnO doping can improve the catalytic performance of catalysts by enhancing the adsorption, dissociation, and desorption of hydrogen species.

To further investigate the effect of ZnO on the catalyst structure, XPS

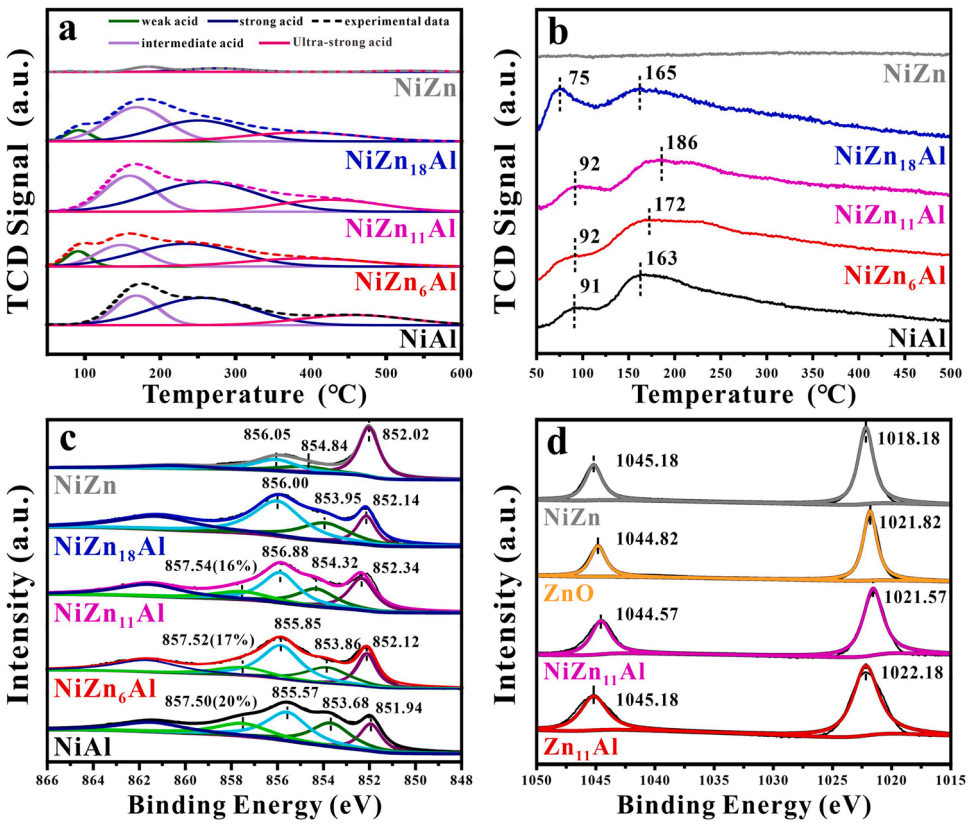

Fig. 2. (a) NH_3-TPD patterns, (b) H_2-TPD patterns, (c) XPS spectra for Ni 2p3/2 of $NiZn_xAl$ catalysts. (d) XPS spectra of Zn 2p3/2 and Zn 2p1/2 of the $NiZn_{11}Al$ catalyst and NiZn catalyst and their respective catalyst carriers.

Table 2
Content of acidic sites in each region of $NiZn_xAl$ measured by NH_3-TPD experiments.

Sample	Acidity [μmol·g^{-1}]				
	Total	Weak	Intermediate	Strong	Very-strong
NiZn	74	2	26	35	11
$NiZn_{18}Al$	596	32	237	208	119
$NiZn_{11}Al$	709	0	207	361	141
$NiZn_6Al$	551	42	124	270	115
NiAl	583	0	145	312	126

spectroscopy was employed to evaluate the electronic interaction between Ni and ZnO in $NiZn_xAl$ catalysts. The XPS spectra of Ni 2p3/2 on different catalysts are shown in Fig. 2c. In the NiAl catalyst, the peak at 851.94 eV corresponds to metallic Ni^0, while the peaks at 853.68 eV and 855.57 eV are attributed to NiO or Ni^{2+}. The peak at 857.50 eV is assigned to $NiAl_2O_4$ species with a spinel structure, and the peak at 861.56 eV is the satellite peak of divalent Ni [28,51,52]. The percentage of peak area at 857.50 eV gradually decreases with the increase of ZnO, indicating that the introduction of ZnO effectively inhibits the formation of $NiAl_2O_4$ species, and the phenomenon is also supported by H_2-TPR results.

Compared to the NiAl catalyst, the peak of metallic Ni^0 in the $NiZn_6Al$ and $NiZn_{11}Al$ catalysts shifts towards higher binding energy in the presence of ZnO, with a shift of 0.4 eV observed in the $NiZn_{11}Al$ catalyst. The increase in binding energy indicates that a certain amount of ZnO doping will reduce the electron cloud density on the Ni surface. On the other hand, the binding energy of Ni^0 in the $NiZn_{18}Al$ and NiZn catalysts decreases to 852.14 eV and 852.02 eV, respectively, compared to $NiZn_{11}Al$ catalyst, indicating an increase in electron cloud density on the Ni surface upon over-doping with ZnO. This may be related to the direction of electron transfer between Ni and ZnO.

Furthermore, the binding energies of Zn 2p3/2 in ZnO and NiZn catalyst, $Zn_{14}Al$ carrier and $NiZn_{11}Al$ catalyst were compared, as shown in Fig. 2d. The binding energy of Zn 2p3/2 in the $Zn_{14}Al$ carrier is 1022.18 eV, which drops to 1021.57 eV when loaded with Ni, indicating electrons transfer from Ni to ZnO. Conversely, the binding energy of Zn 2p3/2 of ZnO is 1021.82 eV, which increases to 1022.18 eV with the addition of Ni, implying electron transfer from ZnO to Ni. The binding energy of Zn 2p3/2 in $NiZn_xAl$ catalysts exhibits the minimum in $NiZn_{11}Al$ catalyst as the ZnO content increases, as shown in Fig. S2. This shift in binding energy of Ni^0 from $NiZn_{11}Al$ catalyst to NiZn catalyst is attributed to the reversal of the electron transfer direction between Ni and ZnO, which may be relevant to the formation of the Ni-Zn alloy [43].

3.1.3. Morphological analysis

The morphology of the NiAl catalyst, $NiZn_{11}Al$ catalyst, and NiZn catalyst was characterized by high-resolution transmission electron microscopy (HRTEM). The particle size distributions of Ni nanoparticles in the NiAl, $NiZn_{11}Al$, and NiZn catalysts are presented in Fig. 3a, Fig. 3b, and Fig. S3a, respectively. The $NiZn_{11}Al$ catalyst exhibited a smaller particle size range, with Ni nanoparticles mainly concentrated in the range of 5–7 nm, as compared to the NiAl catalyst. This indicates that ZnO promotes the dispersion of Ni. However, when ZnO was over-doped, Ni nanoparticles underwent massive agglomeration, resulting in an average particle size of 180 nm (Fig. S3a). The $NiZn_{11}Al$ catalyst morphology was further analyzed in Fig. 3c, where lattice spacings of 0.203 nm, 0.176 nm, and 0.125 nm were assigned to the Ni (111), Ni (200), and Ni (220) crystal planes, respectively. Lattice spacings of 0.138 nm, 0.191 nm, and 0.248 nm were attributed to the ZnO (112), ZnO (102), and ZnO (101) crystal planes. The shaded area in the figure shows overlapping crystal faces and distorted lattice streaks between Ni (200) and ZnO (112), suggesting the formation of a Ni-ZnO interface.

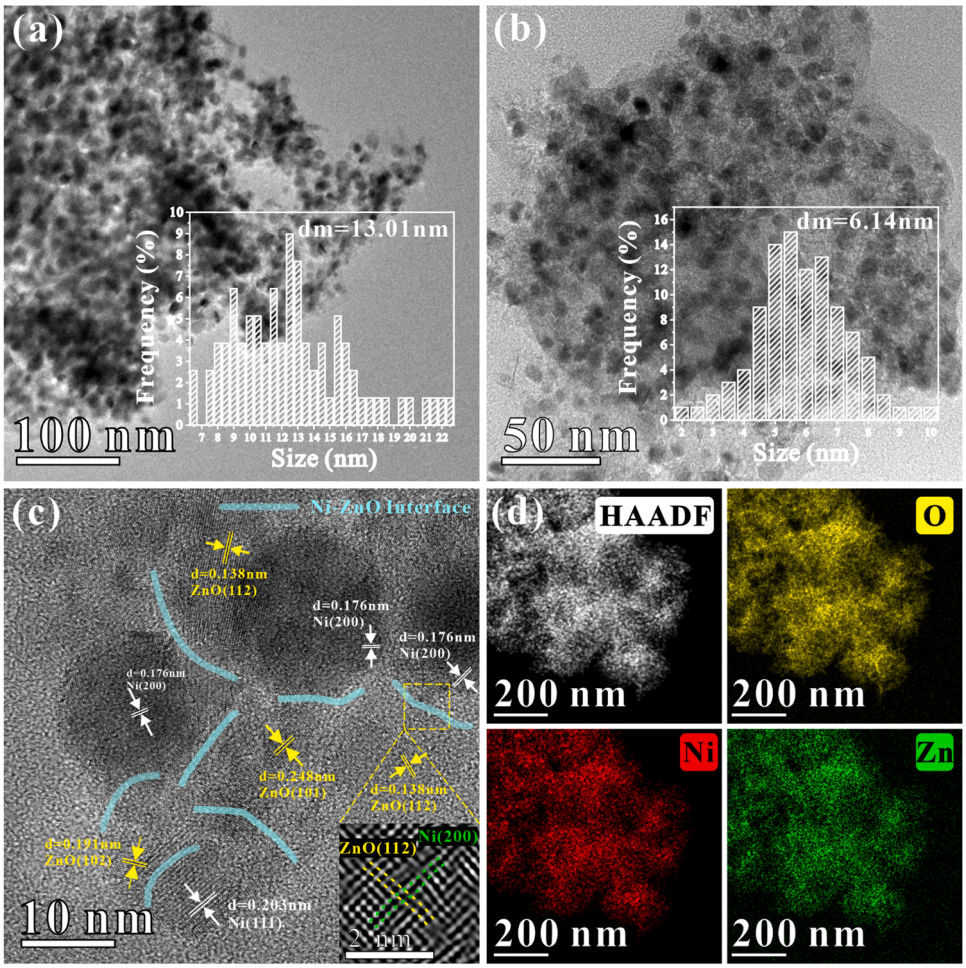

Fig. 3. TEM images of (a) NiAl catalyst, (b, c) $NiZn_{11}Al$ catalyst. (d) $NiZn_{11}Al$ catalyst with the elemental mapping of Ni, Zn.

Previous studies have demonstrated that the Ni-ZnO interface inhibits the aggregation of Ni nanoparticles and promotes electron transfer between Ni and ZnO [31]. Elemental mapping in Fig. 3d further confirms the high dispersion of Ni and the intimate contact between Ni and ZnO on the $NiZn_{11}Al$ catalyst surface. In the NiZn catalyst, the Ni-Zn alloy can be observed in Fig. S3b, where the lattice spacing of Ni (111) expands from 0.203 nm to 0.210 nm in the shaded section. This is due to the entry of Zn atoms into the Ni lattice to form Ni-Zn alloy, which widens the Ni lattice spacing [53]. This finding is consistent with the previous XRD and H_2-TPR results.

3.2. Evaluation of catalytic activity

3.2.1. Activity test: Hydrogenation of NPCZ

The catalytic performance of $NiZn_xAl$ catalysts was evaluated via the hydrogenation of NPCZ. This process involves three consecutive steps that ultimately result in the production of 4H-NPCZ, 8H-NPCZ, and 12H-NPCZ [54]. Scheme 1 illustrates the hydrogenation process of NPCZ. Fig. 4a and Fig. S4 depict the NPCZ hydrogenation of $NiZn_xAl$ catalysts with different ZnO contents. It is noteworthy that the NiAl catalyst achieved saturated hydrogenation of NPCZ in approximately 50 min. The introduction of an appropriate amount of ZnO led to improved catalytic performance for both the $NiZn_6Al$ and $NiZn_{11}Al$ catalysts. The best hydrogenation activity was observed in the $NiZn_{11}Al$ catalyst, which yielded 100% 12H-NPCZ within 25 min. However, the activity of the catalysts decreased significantly with the addition of excess ZnO. For instance, in the $NiZn_{18}Al$ catalyst, the yield of 12H-NPCZ was only 5% at 90 min, while the NiZn catalyst was inactive for catalytic hydrogenation of NPCZ. Table 3 compares the hydrogenation activity between the catalysts presented in this work and those reported in the literature. The $NiZn_{11}Al$ catalyst exhibited better catalytic performance than the commercial 0.5 wt% Ru/Al_2O_3 catalyst [27] and the previously reported catalysts under the same conditions. Furthermore, the calculated hydrogen uptake efficiency of the $NiZn_{11}Al$ catalyst was 18.41 mmol $H_2 \cdot g_{cat}^{-1} \cdot min^{-1}$, which is significantly higher than other reported catalysts.

The step-by-step hydrogenation of NPCZ has been simplified to a first-order reaction. The kinetic results of the hydrogenation at 130–160 °C and 7 MPa were fitted using MATLAB software. The kinetic constants at each temperature are shown in Table 4. As shown in Fig. 4c-

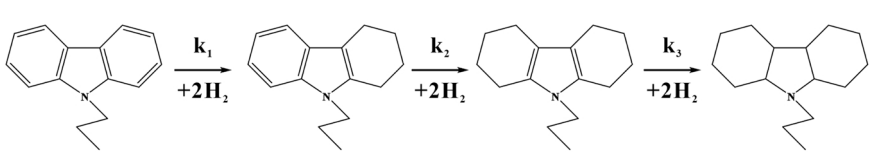

Scheme 1. Hydrogenation process for the conversion of NPCZ to 12H-NPCZ.

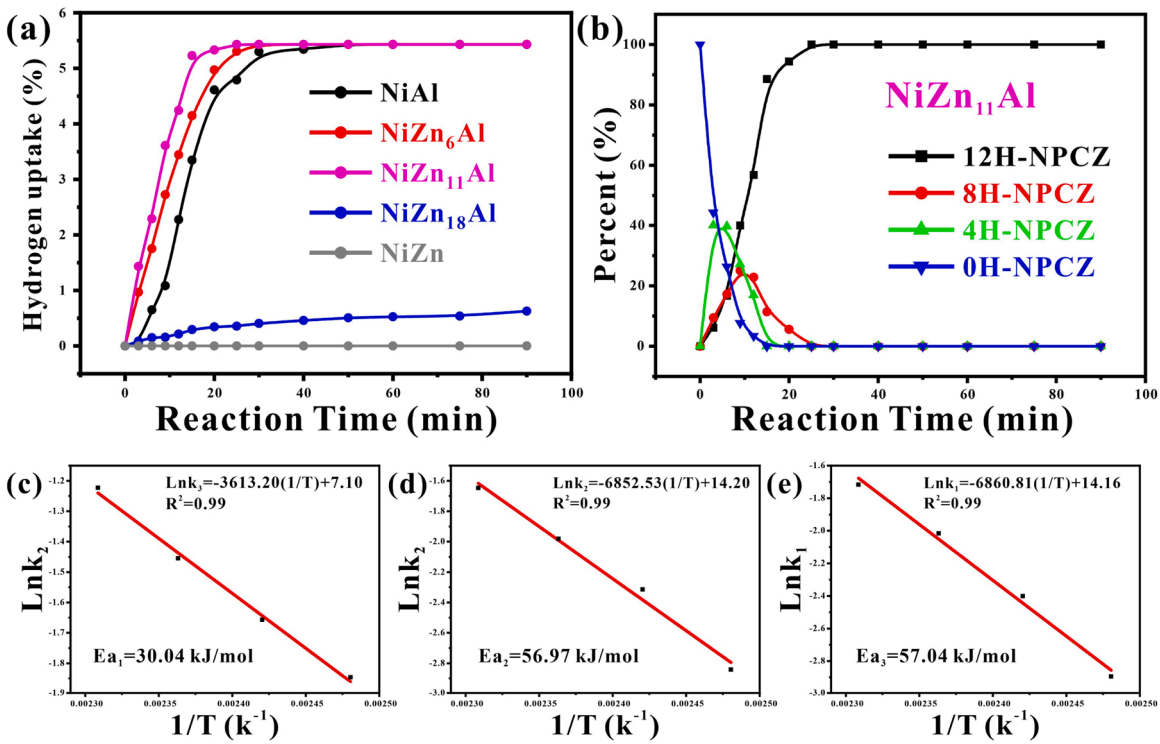

Fig. 4. (a) Hydrogen uptake curves for NPCZ hydrogenation catalyzed by partial $NiZn_xAl$ catalysts at 150 °C and 7 MPa H_2. (b) Time-dependent product distribution for NPCZ over $NiZn_{11}Al$ catalyst (150 °C, 7 MPa H_2). Arrhenius plots of experimental rate constants for each stage of NPCZ hydrogenation catalyzed by $NiZn_{11}Al$ catalyst at 130−160 °C and 7 MPa. (a) NPCZ→4H-NPCZ, (b) 4H-NPCZ→8H-NPCZ, (c) 8H-NPCZ→12H-NPCZ.

Table 3
The activity of different catalysts for the hydrogenation of NPCZ.

Catalysts	Conditions[a]	Time to achieve saturated hydrogenation/ min	Hydrogen absorption efficiency/mmol $H_2 \cdot g_{cat}^{-1} \cdot min^{-1}$	References
$NiZn_{11}Al$	150 °C, 7 MPa H_2	25	18.41	This work
$NiZn_6Al$	150 °C, 7 MPa H_2	30	13.10	This work
NiAl	150 °C, 7 MPa H_2	50	9.33	This work
70 wt% Ni/ SiO_2-Al_2O_3	150 °C, 7 MPa H_2	60	4.76	Ding et al. [27]
0.5 wt% Ru/ Al_2O_3	150 °C, 7 MPa H_2	240	1.87	Ding et al. [27]
5 wt% Ru/ Al_2O_3	150 °C, 7 MPa H_2	30	4.78	Yang et al. [54]
0.34 wt% Ru/WO_3	170 °C, 8 MPa H_2	180	4.57	Li et al. [55]
1 wt% Pd/ CeO_2-Al_2O_3	150 °C, 7 MPa H_2	180	1.02	Li et al. [56]
2.5 wt% Ru-2.5 wt% Pd/ Al_2O_3	150 °C, 7 MPa H_2	420	1.42	Zhu et al. [57]

[a] The weight ratios of catalyst to reactant were all 1/10.

e, the reaction activation energies Ea_1, Ea_2, and Ea_3 calculated from the Arrhenius equation are 30.04 kJ/mol, 56.97 kJ/mol, and 57.04 kJ/mol, respectively. The hydrogenation activation energy of the $NiZn_{11}Al$ catalyst in the NPCZ→4H-NPCZ stage was significantly lower than that of the Ru/WO_3 [55] catalyst (70.09 kJ/mol).

Table 4
Equilibrium constants for each stage of NPCZ hydrogenation catalyzed by $NiZn_{11}Al$ catalyst under different conditions.

Conditions	k_1/min^{-1}	k_2/min^{-1}	k_3/min^{-1}
130 °C, 7 MPa H_2	0.1578	0.0583	0.0553
140 °C, 7 MPa H_2	0.1907	0.0988	0.0906
150 °C, 7 MPa H_2	0.2334	0.1378	0.1332
160 °C, 7 MPa H_2	0.2943	0.1925	0.1797

3.2.2. *Stability of catalysts*

Ensuring the stability of catalysts is essential for practical industrial production [58]. One of the critical factors limiting the large-scale application of Ni-based catalysts is deactivation caused by nickel nanoparticle aggregation. To explore the stability of the catalyst, 10 cycles of NPCZ hydrogenation were conducted on the $NiZn_{11}Al$ catalyst. The hydrogen uptake of 10 cycles is illustrated in Fig. 5a. The catalytic activity of the $NiZn_{11}Al$ catalyst was stable over ten cycles, and 100% 12H-NPCZ could be obtained within 120 min. The stability of the catalyst was significantly enhanced compared to the study by Ding et al. [27]. The decrease in catalytic activity compared with the first cycle could be attributed to the partial oxidation of Ni when exposed to air. As shown in Fig. 5b, the diffraction peaks at 37.2° and 62.9° in the $NiZn_{11}Al$ catalyst were attributed to the (111) and (220) crystal planes of NiO (PDF#47–1049), respectively. These diffraction peaks for NiO species were increased after 10 hydrogenation cycles, while the Ni^0 diffraction peaks became weakened, indicating that the active component were oxidized during catalysis or washing operation, which might be one of the reasons that leads to the decreased catalytic activity of the reused catalyst. In Fig. 5c, the binding energy of Ni^0 for $NiZn_{11}Al$-C and $NiZn_{11}Al$-F catalysts are 852.50 and 852.34 eV, respectively, and the intensity of the characteristic peak of $NiZn_{11}Al$-C catalyst is significantly decreased, which indicates that the Ni is partially oxidized after ten cycles of this catalyst. The changes in the pore structure parameters for

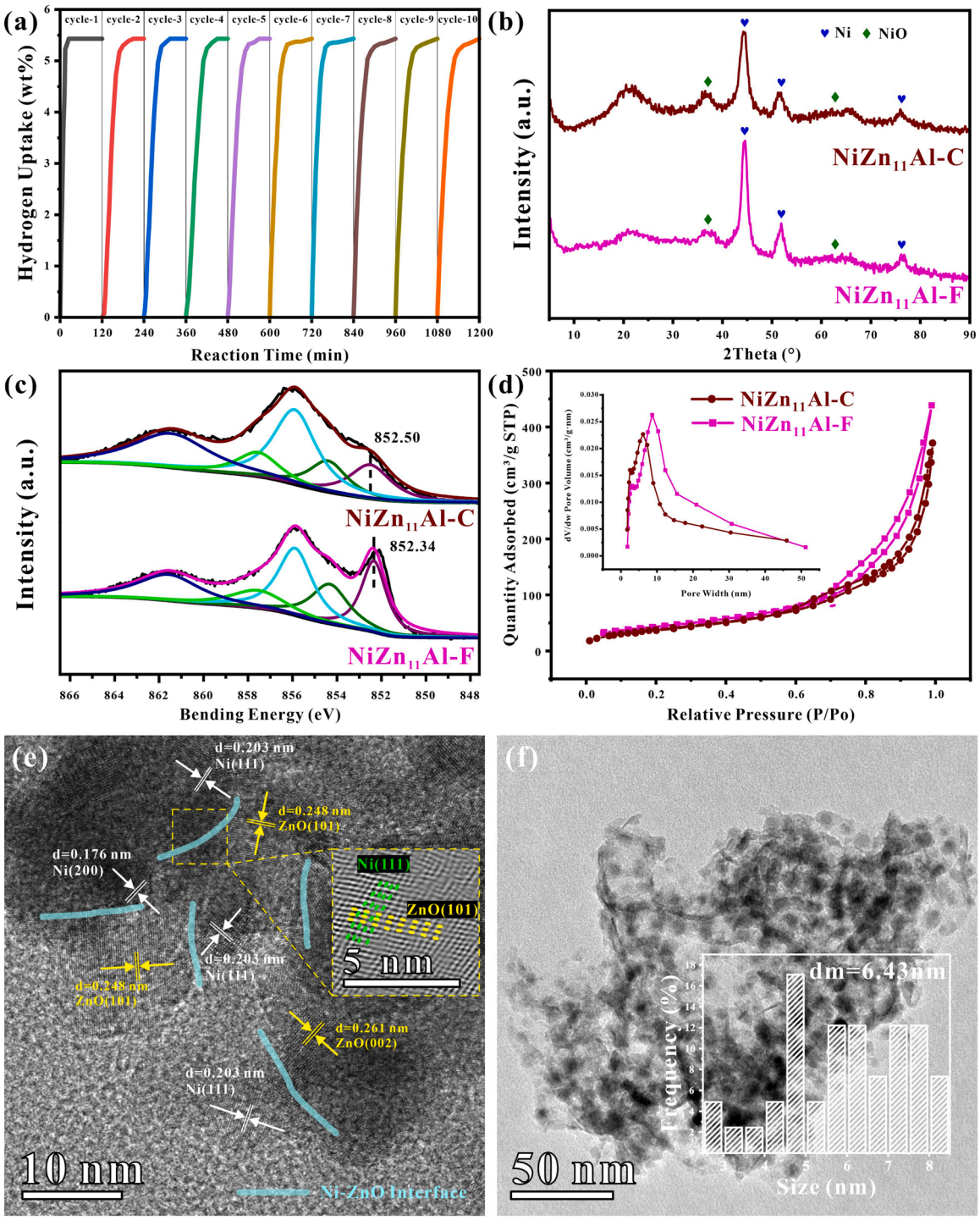

Fig. 5(. a) Hydrogen uptake of NPCZ hydrogenation over $NiZn_{11}Al$ catalyst for ten repeated cycles (150 °C, 7 MPa H_2). Comparative characterization of $NiZn_{11}Al$-F catalyst and $NiZn_{11}Al$-C catalyst: (b) XRD, (c) XPS, (d) BET, (e-f) HRTEM.

Table 5
Main structural parameters of fresh and 10 hydrogenation cycles of $NiZn_{11}Al$ catalysts.

Sample	BET Surface Area (m^2/g):	Pore Volume (cm^3/g)[a]	Average Pore Size (nm)[a]
$NiZn_{11}Al$-F	155	0.68	13.3
$NiZn_{11}Al$-C	144	0.57	12.4

[a] Pore volume and average pore size were calculated according to the BJH method.

the fresh and reused catalyst after 10 cycles are displayed in Fig. 5d and Table 5. The specific surface area and pore volume of the spent catalysts were 144 m^2/g and 0.57 cm^3/g, demonstrating that the catalyst maintained the mesoporous structure after 10 cycles of hydrogenation. The HRTEM image of $NiZn_{11}Al$-C is shown in Fig. 5e, the results showed that the interface remained stable after 10 catalytic hydrogenation cycles, implying that Ni nanoparticles still displayed high dispersion on the cycled catalysts. Fig. S5 shows that there was no significant aggregation of the catalyst after 10 cycles. The average particle size of $NiZn_{11}Al$-C was calculated to be 6.43 nm (Fig. 5f). The excellent stability of the

$NiZn_{11}Al$ catalyst could be attributed to the stable Ni-ZnO interface formed by the interaction between Ni and ZnO. Consequently, the $NiZn_{11}Al$ catalyst shows great potential for industrial applications.

3.3. Catalytic mechanism

3.3.1. DFT calculations

DFT calculations were conducted to simulate two models of Ni_{13} and Ni_7Zn_6 clusters adsorbed on the ZnO(100) surface. The main focus of this study was to investigate the electron distribution between the metal clusters and the ZnO(100) interface. Fig. S6 depicts the top and side views of the two clusters placed on the surface of ZnO(100). The Ni_{13}/ZnO(100) surface represents $NiZn_xAl$ catalysts with a small amount of ZnO doping, where x is less than 11. On the other hand, Ni_7Zn_6/ZnO (100) represents $NiZn_xAl$ catalysts with excessive ZnO doping, resulting in the formation of a Ni-Zn alloy.

We analyzed the electronic structure of Ni_{13}/ZnO(100) and Ni_7Zn_6/ZnO(100) surfaces, as shown in Fig. 6. Specifically, Fig. 6a and Fig. 6e illustrate the charge density difference of Ni_{13}/ZnO(100) and Ni_7Zn_6/ZnO(100) surfaces, respectively. A comparison of the two figures indicates that the charge on the Ni_7Zn_6/ZnO(100) surface mainly concentrates at the interface of Ni_7Zn_6 clusters adsorbed on the ZnO(100) slab. Similarly, the 2D display charge density difference on the Ni_{13}/ZnO (100) surface in Fig. 6b shows the presence of a small amount of charge at the interface. However, the charge at the Ni_7Zn_6/ZnO(100) interface in Fig. 6f increases significantly, and the charge in the ZnO(100) slab decreases, indicating a charge transfer from ZnO to the Ni_7Zn_6 cluster.

Fig. 6c and 6g present the planar-average charge difference density plots for Ni_{13}/ZnO(100) and Ni_7Zn_6/ZnO(100) surfaces, with a focus on observing the charge variation curve with the z-axis. The comparison reveals that the charge increases around the z-axis of 6 Å in Fig. 6g. Additionally, Fig. 6d and 6h display the partial density of states (PDOS) of the Ni_{13}/ZnO(100) and Ni_7Zn_6/ZnO(100) surfaces. From the D-orbital PDOS of Ni, it can be seen that the PDOS of Ni_7Zn_6/ZnO(100) surface moves down the Fermi level. Simultaneously, the charge number of the valence band part of its s-orbital increases.

Furthermore, Bader charge analysis was performed on the Ni_{13}/ZnO (100) and Ni_7Zn_6/ZnO(100) surfaces. Notably, the average value of the Bader charge of Ni in the Ni_{13}/ZnO(100) surface is 9.95, while the average value of the Bader charge of Ni in the Ni_7Zn_6/ZnO(100) surface is 10.09. Through these electronic structure analyses, we infer that electrons in the Ni_{13}/ZnO(100) surface flow from Ni_{13} clusters to the ZnO slab, while electrons on the Ni_7Zn_6/ZnO(100) surface move from the ZnO slab to the Ni_7Zn_6 cluster. The XPS characterization supports this notion, indicating that electrons are transferred from Ni to ZnO when a small amount of ZnO is doped. As the amount of ZnO doping increases, the electron flow changes from ZnO to Ni, promoting the electron-rich state around Ni.

3.3.2. Mechanism of the catalyst

Electron transfer is the basis of the synergy between active ingredients in NiZn-based catalysts. XPS characterization and DFT calculations demonstrate that when a small amount of ZnO is doped into Ni-based catalysts, electrons are transferred from Ni to the ZnO surface. As a result, $Ni^{\delta+}$ with low electron cloud density appears on the catalyst surface [30]. Conversely, when ZnO is over-doped, XRD and H_2-TPR results indicate that a Ni-Zn alloy phase forms (Fig. 2c, d). In Ni-Zn alloy, electrons transfer from Zn to Ni due to the higher electronegativity of Ni (1.91) than Zn (1.65) [43,59]. This leads to an increase in electron cloud density on the Ni surface and a decrease in the content of $Ni^{\delta+}$ species.

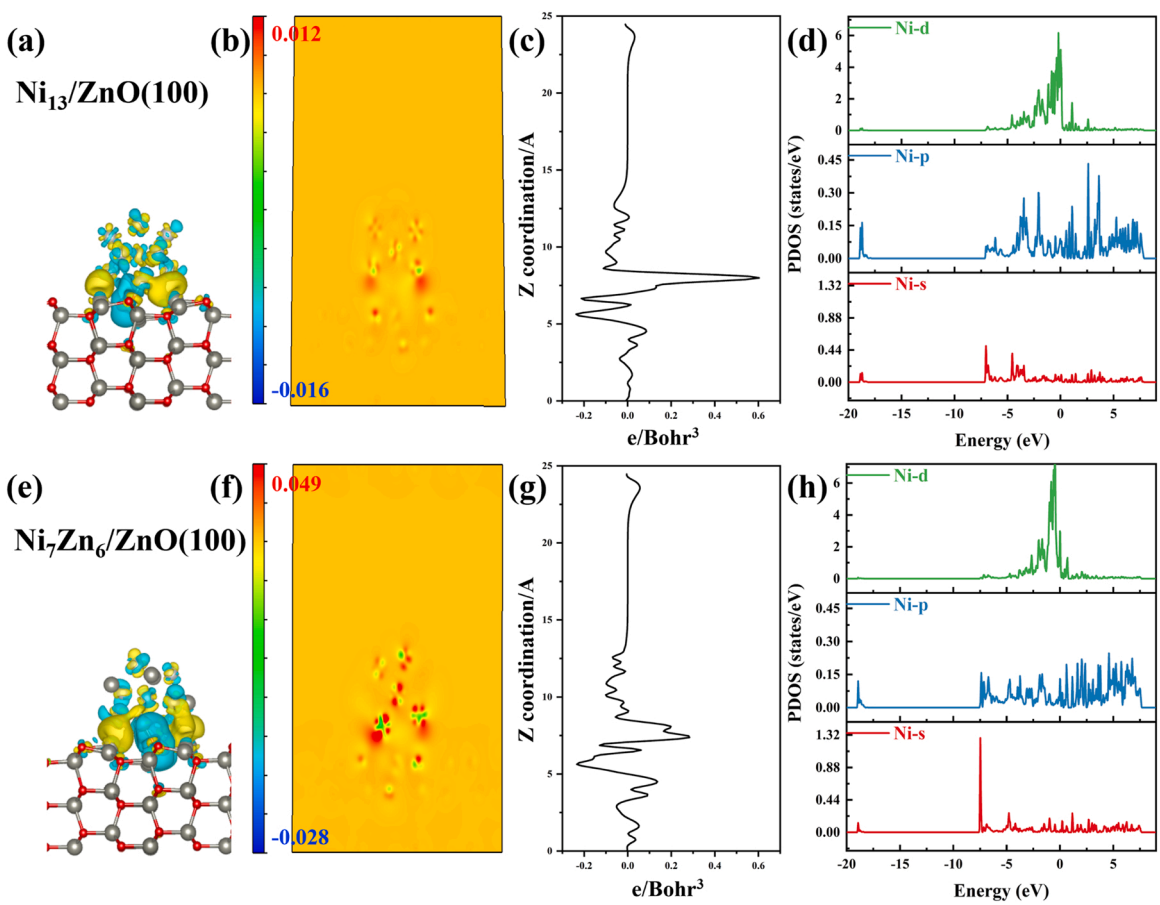

Fig. 6. (a,e) The charge density difference, (b,f) the 2D display charge density difference, (c,g) the planar-average charge difference density plots, (d,h) the partial density of states (PDOS) for Ni_{13}/ZnO(100) and Ni_7Zn_6/ZnO(100).

The production of $Ni^{\delta+}$ enhances the strength and density of the acidic sites on the surface, promoting the anisotropic splitting of H_2 into H^+ and H^- and increasing the variety of active hydrogen [60,61]. This explains why $NiZn_{11}Al$ catalyst has the highest activity among all catalysts.

Despite having a smaller specific surface area than the NiAl and $NiZn_6Al$ catalyst, the $NiZn_{11}Al$ catalyst shows better catalytic activity, attributed to the higher ZnO content favoring the formation of the Ni-ZnO interface. Such an interface facilitated the dispersion and electron transfer of Ni. $NiZn_{11}Al$ catalyst provided the highest total acid content due to a large amount of electron transfer from Ni to ZnO, which is favorable for the adsorption of the organic base NPCZ. The significant amount of $Ni^{\delta+}$ formed also results in a more robust hydrogen adsorption capacity. Compared to the $NiZn_{11}Al$ catalyst, the Ni^0 in the $NiZn_{18}Al$ catalyst exhibits a shift towards a lower binding energy, thereby indicating a higher electron cloud density on the surface of Ni nanoparticles in the $NiZn_{18}Al$ catalyst. However, this change is not conducive to the stability of the acidic sites and active hydrogen species, which are crucial for catalysis. In contrast, the low specific surface area of the NiZn catalyst renders it catalytically inactive.

Based on the experimental results and characterization analysis, we propose a catalytic mechanism for the $NiZn_{11}Al$ catalyst in the NPCZ hydrogenation reaction, as shown in Fig. 7. At the Ni-ZnO interface, Ni and ZnO exist in the form of $Ni^{\delta+}$ and $(ZnO)^{\delta-}$, respectively, due to the transfer of electrons from Ni to ZnO. H_2 is activated in the presence of $Ni^{\delta+}$ and splits anisotropically into H^+ and H^-. Due to the electron-deficient character of $Ni^{\delta+}$, it tends to be more coordinated with electron-rich atoms. In the organic base NPCZ, the N atom is not an electron donor in the hydrogenation of NPCZ, as the lone pair of electrons on the N atom is involved in the conjugation of the aromatic ring in NPCZ [62]. Instead, the electron-rich π-bonds on the benzene ring on both sides combine with $Ni^{\delta+}$ via charge attraction to trigger the hydrogenation reaction. As shown in Scheme I, the hydrogenation reaction of NPCZ starts with the benzene ring on one side. Due to the electron-giving effect of the N atom, the C atom closer to the N atom has a higher electron cloud density and becomes the preferential target for the attack of H^+. After hydrogenating the first benzene ring, the other benzene ring undergoes hydrogenation similarly. Finally, H^+ and H^- attack the double bonds on the pyrrole ring. After the hydrogenation of NPCZ is complete, the catalyst is separated from the substrate and enters the next cycle. It is worth noting that the formation of a large amount of $Ni^{\delta+}$ in the $NiZn_{11}Al$ catalyst makes NPCZ more favorable to adsorption on the catalyst surface and significantly reduces the activation energy of the hydrogenation reaction.

4. Conclusion

In summary, a series of $NiZn_xAl$ catalysts were prepared using co-precipitation, which were then tested for catalytic hydrogenation of NPCZ. This study provides an insight into the effect of ZnO content on the performance of $NiZn_xAl$ catalysts and identifies $NiZn_{11}Al$ as the most promising catalyst for catalytic hydrogenation of NPCZ, owing to its unique Ni-ZnO interface. The excellent catalytic hydrogenation performance was attributed to the moderately interaction between Ni and ZnO. This interaction promoted the formation of a Ni-ZnO interface which not only enhanced the dispersion of Ni nanoparticles, promoted the electron transfer from Ni to ZnO, improved the adsorption and stability of reaction intermediates and hydrogen species, but also inhibited the agglomeration of active components. Specifically, excessive ZnO addition caused a drastic reduction in the specific surface area of the catalyst and promoted the formation of Ni-Zn alloy. The presence of Ni-Zn alloy resulted in electron transfer from Zn to Ni, increasing the electron cloud density on the Ni surface, reducing the acidity of the

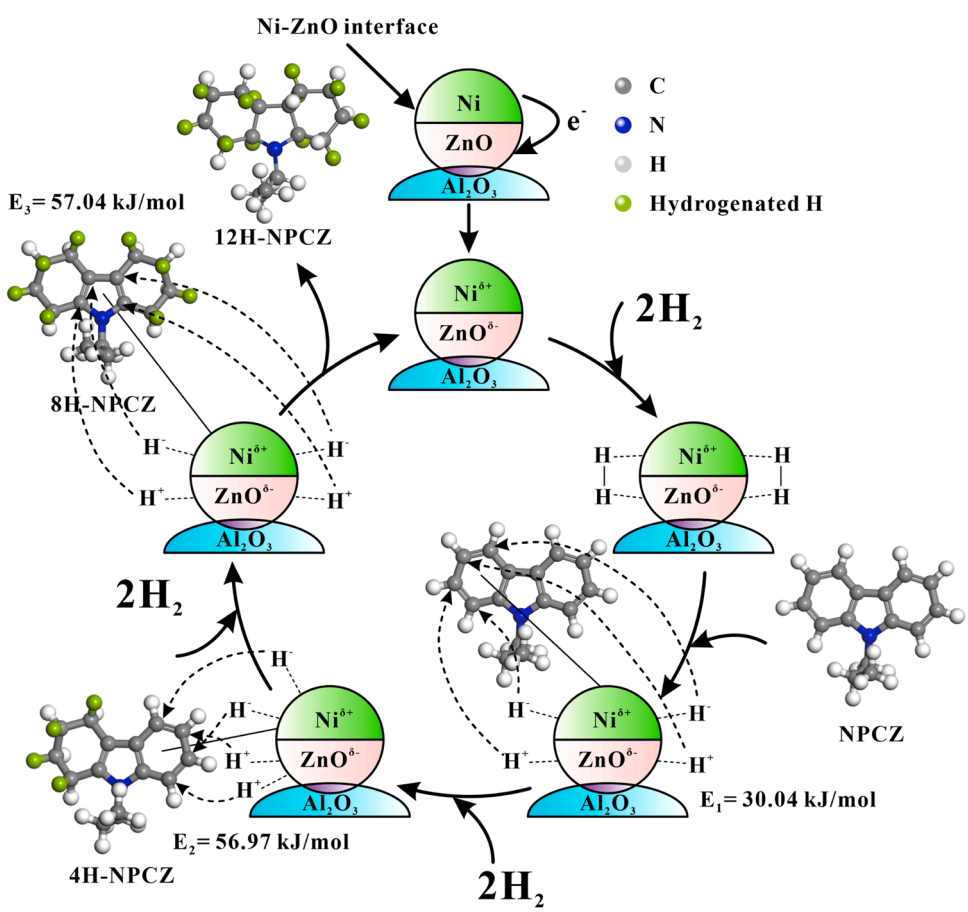

Fig. 7. Plausible pathway for the hydrogenation of NPCZ into 12H-NPCZ over Ni−ZnO interface in $NiZn_{11}Al$ catalyst.

catalyst, weakening the stability of the hydrogen species and ultimately decreasing the hydrogenation activity of the catalyst. The $NiZn_{11}Al$ catalyst, with suitable ZnO doping, exhibited the best hydrogenation activity and cycle stability. In addition, the active metal Ni and the additive ZnO are both available at a reasonable cost, the preparation process is based on a simple co-precipitation method, which makes the $NiZn_{11}Al$ catalyst economically feasible and thus implies great potential for industrial applications.

CRediT authorship contribution statement

Yinheng Zhao: Investigation, Writing – original draft. **Chenggen Li & Ting Zhu:** Writing – review & editing, Visualization. **Yuanzheng Zhu & Li Liu:** Data curation. **Yuan Dong:** Methodology. **Hansong Cheng:** Resources, Supervision. **Ming Yang:** Supervision, Conceptualization.

Declaration of Competing Interest

The authors declare that they have no known competing financial interests or personal relationships that could have appeared to influence the work reported in this paper.

Data Availability

Data will be made available on request.

Acknowledgements

The authors gratefully acknowledge the financial support from the Key Research and Development Program of Hubei Province (No. 2021BAD005, 2022BAA090, 2022BAA091), the National Key Research and Development Program of China (No. 2018YFB1502903), the Zhejiang Provincial Natural Science Foundation of China (No. LGG20B030001), the National Natural Science Foundation of China (No. 21875225).

Appendix A. Supporting information

Supplementary data associated with this article can be found in the online version at doi:10.1016/j.apcatb.2023.122792.

References

[1] C. Tarhan, M.A. Çil, A study on hydrogen, the clean energy of the future: hydrogen storage methods, J. Energy Storage 40 (2021) 102676–102685.
[2] J.C. Crittenden, H.S. White, Harnessing energy for a sustainable world, J. Am. Chem. Soc. 132 (2010) 4503–4505.
[3] L. Wang, D. Wang, Y. Li, Single-atom catalysis for carbon neutrality, Carbon Energy 4 (2022) 1021–1079.
[4] Y. Feng, J. Han, M. Xu, X. Liang, T. Jiang, H. Li, Z.L. Wang, Blue energy for green hydrogen fuel: a self-powered electrochemical conversion system driven by triboelectric nanogenerators, Adv. Energy Mater. 12 (2022) 2103143–2103150.
[5] Q.-L. Zhu, Q. Xu, Liquid organic and inorganic chemical hydrides for high-capacity hydrogen storage, Energy Environ. Sci. 8 (2015) 478–512.
[6] D. Teichmann, W. Arlt, P. Wasserscheid, R. Freymann, A future energy supply based on liquid organic hydrogen carriers (LOHC), Energy Environ. Sci. 4 (2011) 2767–2773.
[7] M. Niermann, S. Drünert, M. Kaltschmitt, K. Bonhoff, Liquid organic hydrogen carriers (LOHCs) – techno-economic analysis of LOHCs in a defined process chain, Energy Environ. Sci. 12 (2019) 290–307.
[8] D. Teichmann, W. Arlt, P. Wasserscheid, Liquid organic hydrogen carriers as an efficient vector for the transport and storage of renewable energy, Int. J. Hydrog. Energy 37 (2012) 18118–18132.
[9] P. Preuster, C. Papp, P. Wasserscheid, Liquid organic hydrogen carriers (LOHCs): toward a hydrogen-free hydrogen economy, Acc. Chem. Res 50 (2017) 74–85.
[10] N. Bruckner, K. Obesser, A. Bosmann, D. Teichmann, W. Arlt, J. Dungs, P. Wasserscheid, Evaluation of industrially applied heat-transfer fluids as liquid organic hydrogen carrier systems, Chemsuschem 7 (2014) 229–235.
[11] M. Niermann, A. Beckendorff, M. Kaltschmitt, K. Bonhoff, Liquid organic hydrogen carrier (LOHC) – assessment based on chemical and economic properties, Int. J. Hydrog. Energy 44 (2019) 6631–6654.
[12] A. Haupt, K. Müller, Integration of a LOHC storage into a heat-controlled CHP system, Energy 118 (2017) 1123–1130.
[13] M. Markiewicz, Y.-Q. Zhang, M.T. Empl, M. Lykaki, J. Thöming, P. Steinberg, S. Stolte, Hazard assessment of quinaldine-, alkylcarbazole-, benzene- and toluene-based liquid organic hydrogen carrier (LOHCs) systems, Energy Environ. Sci. 12 (2019) 366–383.
[14] J. Yan, W. Wang, L. Miao, K. Wu, G. Chen, Y. Huang, Y. Yang, Dehydrogenation of methylcyclohexane over Pt Sn supported on Mg Al mixed metal oxides derived from layered double hydroxides, Int. J. Hydrog. Energy 43 (2018) 9343–9352.
[15] A. Moores, M. Poyatos, Y. Luo, R.H. Crabtree, Catalysed low temperature H_2 release from nitrogen heterocycles, N. J. Chem. 30 (2006) 1675–1678.
[16] R.H. Crabtree, Nitrogen-containing liquid organic hydrogen carriers: progress and prospects, ACS Sustain. Chem. Eng. 5 (2017) 4491–4498.
[17] R.H. Crabtree, Hydrogen storage in liquid organic heterocycles, Energy Environ. Sci. 1 (2008) 134–138.
[18] Z. Chen, M. Yang, T. Zhu, Z. Zhang, X. Chen, Z. Liu, Y. Dong, G. Cheng, H. Cheng, 7-ethylindole: a new efficient liquid organic hydrogen carrier with fast kinetics, Int J. Hydrog. Energ. 43 (2018) 12688–12696.
[19] X. Hu, Y. Chen, B. Huang, Y. Liu, H. Huang, Z. Xie, Pd-supported N/S-codoped graphene-like carbons boost quinoline hydrogenation activity, ACS Sustain. Chem. Eng. 7 (2019) 11369–11376.
[20] H. Yu, X. Yang, X. Jiang, Y. Wu, S. Chen, W. Lin, Y. Wu, L. Xie, X. Li, J. Zheng, $LaNi_{5.5}$ particles for reversible hydrogen storage in N-ethylcarbazole, Nano Energy 80 (2021) 105476–105483.
[21] H. Yu, Y. Wu, S. Chen, Z. Xie, Y. Wu, N. Cheng, X. Yang, W. Lin, L. Xie, X. Li, J. Zheng, Pd-modified $LaNi_5$ nanoparticles for efficient hydrogen storage in a carbazole type liquid organic hydrogen carrier, Appl. Catal. B: Environ. 317 (2022) 121720–121728.
[22] L. Ge, M. Qiu, Y. Zhu, S. Yang, W. Li, W. Li, Z. Jiang, X. Chen, Synergistic catalysis of Ru single-atoms and zeolite boosts high-efficiency hydrogen storage, Appl. Catal. B: Environ. 319 (2022) 121958–121968.
[23] W. Xue, H. Liu, B. Zhao, L. Ge, S. Yang, M. Qiu, J. Li, W. Han, X. Chen, Single Rh_1Co catalyst enabling reversible hydrogenation and dehydrogenation of N-ethylcarbazole for hydrogen storage, Appl. Catal. B: Environ. 327 (2023) 122453–122460.
[24] V. Papa, Y. Cao, A. Spannenberg, K. Junge, M. Beller, Development of a practical non-noble metal catalyst for hydrogenation of N-heteroarenes, Nature, Catalysis 3 (2020) 135–142.
[25] C. Li, M. Yang, Z. Liu, Z. Zhang, T. Zhu, X. Chen, Y. Dong, H. Cheng, Ru–Ni/Al_2O_3 bimetallic catalysts with high catalytic activity for N-propylcarbazole hydrogenation, Catal. Sci. Technol. 10 (2020) 2268–2276.
[26] T.A. Le, J.K. Kang, E.D. Park, Active Ni/SiO_2 catalysts with high Ni content for benzene hydrogenation and CO methanation, Appl. Catal. A: Gen. 581 (2019) 67–73.
[27] Y. Ding, Y. Dong, H. Zhang, Y. Zhao, M. Yang, H. Cheng, A highly adaptable Ni catalyst for liquid organic hydrogen carriers hydrogenation, Int. J. Hydrog. Energy 46 (2021) 27026–27036.
[28] H. Liu, C. Zhou, W. Li, W. Li, M. Qiu, X. Chen, H. Wang, Y. Sun, Ultralow Rh bimetallic catalysts with high catalytic activity for the hydrogenation of N-ethylcarbazole, ACS Sustain. Chem. Eng. 9 (2021) 5260–5267.
[29] Y. Wu, H. Yu, Y. Guo, Y. Zhang, X. Jiang, B. Sun, K. Fu, J. Chen, Y. Qi, J. Zheng, X. Li, Promoting hydrogen absorption of liquid organic hydrogen carriers by solid metal hydrides, J. Mater. Chem. A 7 (2019) 16677–16684.
[30] J. Wang, H. Jin, W.-H. Wang, Y. Zhao, Y. Li, M. Bao, Ultrasmall Ni–ZnO/SiO_2 synergistic catalyst for highly efficient hydrogenation of $NaHCO_3$ to formic acid, ACS Appl. Mater. Interfaces 12 (2020) 19581–19586.
[31] P.S. Murthy, Z. Wang, L. Wang, J. Zhao, Z. Wang, W. Liang, J. Huang, Improved CO_2 hydrogenation on Ni–ZnO/MCM-41 catalysts with cooperative Ni and ZnO sites, Energy Fuels 34 (2020) 16320–16329.
[32] J. Wu, T. Li, G. Meng, Y. Xiang, J. Hai, B. Wang, Carbon nanofiber supported Ni–ZnO catalyst for efficient and selective hydrogenation of pyrolysis gasoline, Catal. Sci. Technol. 11 (2021) 4216–4225.
[33] G. Kresse, J. Furthmuller, Efficient iterative schemes for ab initio total-energy calculations using a plane-wave basis set, Phys. Rev. B 54 (1996) 11169–11186.
[34] G. Kresse, J. Furthmuller, Efficiency of ab-initio total energy calculations for metals and semiconductors using a plane-wave basis set, Comput. Mater. Sci. 6 (1996) 15–50.
[35] J.P. Perdew, K. Burke, M. Ernzerhof, Generalized gradient approximation made simple, Phys. Rev. Lett. 77 (1996) 3865–3868.
[36] P.E. Blochl, Projector augmented-wave method, Phys. Rev. B 50 (1994) 17953–17979.
[37] D. Guo, Y. Fu, F. Bu, H. Liang, L. Duan, Z. Zhao, C. Wang, A.M. El-Toni, W. Li, D. Zhao, Monodisperse ultrahigh nitrogen-containing mesoporous carbon nanospheres from melamine-formaldehyde resin, Small Methods 5 (2021) 2001137–2001146.
[38] Ky Shimomura, K. Ogawa, M. Oba, Y. Kotera, Copper oxide-zinc oxide-alumina catalyst: the structure of a copper oxide-zinc oxide-alumina catalyst for methanol synthesis, J. Catal. 52 (1978) 191–205.
[39] J.B. Friedrich, M.S. Wainwright, D.J. Young, Methanol synthesis over Raney copper-zinc catalysts: I. Activities and surface properties of fully extracted catalysts, J. Catal. 80 (1983) 1–13.
[40] F.H. Wong, T.J. Tiong, L.K. Leong, K.-S. Lin, Y.H. Yap, Effects of ZnO on characteristics and selectivity of coprecipitated Ni/ZnO/Al_2O_3 catalysts for partial hydrogenation of sunflower oil, Ind. Eng. Chem. Res. 57 (2018) 3163–3174.
[41] X. Meng, Y. Yang, L. Chen, M. Xu, X. Zhang, M. Wei, A control over hydrogenation selectivity of furfural via tuning exposed facet of Ni catalysts, ACS Catal. 9 (2019) 4226–4235.

[42] X. Kong, Y. Zhu, H. Zheng, Y. Zhu, Z. Fang, Inclusion of Zn into metallic Ni enables selective and effective synthesis of 2,5-Dimethylfuran from bioderived 5-Hydroxymethylfurfural, ACS Sustain. Chem. Eng. 5 (2017) 11280–11289.
[43] W. Wang, X. Li, Y. Zhang, R. Zhang, H. Ge, J. Bi, M. Tang, Strong metal–support interactions between Ni and ZnO particles and their effect on the methanation performance of Ni/ZnO, Catal. Sci. Technol. 7 (2017) 4413–4421.
[44] B.W. Hoffer, A. Dick van Langeveld, J.-P. Janssens, R.L.C. Bonné, C.M. Lok, J. A. Moulijn, Stability of highly dispersed Ni/Al_2O_3 catalysts: effects of pretreatment, J. Catal. 192 (2000) 432–440.
[45] Z. Chen, M. Zhang, J. Hua, M. Yang, Y. Dong, H. Cheng, Remarkable activity of Pd catalyst supported on alumina synthesized via a hydrothermal route for hydrogen release of perhydro-N-propylcarbazole, Int. J. Hydrog. Energy 46 (2021) 9718–9729.
[46] L. Shi, Y. Zhou, S. Qi, K.J. Smith, X. Tan, J. Yan, C. Yi, Pt catalysts supported on H_2 and O_2 plasma-treated Al_2O_3 for hydrogenation and dehydrogenation of the liquid organic hydrogen carrier pair dibenzyltoluene and perhydrodibenzyltoluene, ACS Catal. 10 (2020) 10661–10671.
[47] Y. Zi, M. Lange, C. Schultz, I. Vilotijevic, Latent nucleophiles in lewis base catalyzed enantioselective N-allylations of N-heterocycles, Angew. Chem. Int Ed. Engl. 58 (2019) 10727–10731.
[48] W. Li, X. Nie, X. Jiang, A. Zhang, F. Ding, M. Liu, Z. Liu, X. Guo, C. Song, ZrO_2 support imparts superior activity and stability of Co catalysts for CO_2 methanation, Appl. Catal. B: Environ. 220 (2018) 397–408.
[49] E. Janiszewska, M. Kot, M. Zieliński, Modification of silica with NH_4^+ agents to prepare an acidic support for iridium hydrogenation catalyst, Microporous Mesoporous Mater. 255 (2018) 94–102.
[50] S. Ewald, S. Standl, O. Hinrichsen, Characterization of nickel catalysts with transient methods, Appl. Catal. A: Gen. 549 (2018) 93–101.
[51] Z. Hou, Characterization of Ca-promoted Ni/α-Al_2O_3 catalyst for CH_4 reforming with CO_2, Appl. Catal. A: Gen. 253 (2003) 381–387.
[52] S. Kirumakki, B. Shpeizer, G. Sagar, K. Chary, A. Clearfield, Hydrogenation of naphthalene over NiO/SiO_2–Al_2O_3 catalysts: structure–activity correlation, J. Catal. 242 (2006) 319–331.
[53] X. Meng, L. Wang, L. Chen, M. Xu, N. Liu, J. Zhang, Y. Yang, M. Wei, Charge-separated metal-couple-site in NiZn alloy catalysts towards furfural hydrodeoxygenation reaction, J. Catal. 392 (2020) 69–79.
[54] M. Yang, Y. Dong, S. Fei, Q. Pan, G. Ni, C. Han, H. Ke, Q. Fang, H. Cheng, Hydrogenation of N-propylcarbazole over supported ruthenium as a new prototype of liquid organic hydrogen carriers (LOHC), RSC Adv. 3 (2013) 24877–24881.
[55] P. Li, Y. Dong, Y. Ding, H. Zhang, M. Yang, H. Cheng, Effect of hydrogen spillover on the surface of tungsten oxide on hydrogenation of cyclohexene and N-propylcarbazole, Int. J. Hydrog. Energy 46 (2021) 3945–3953.
[56] C. Li, Q. Zhang, Z. Xu, L. Liu, T. Zhu, Z. Chen, Y. Dong, M. Yang, Ce-promoted highly active bifunctional Pd/Al_2O_3 catalyst for reversible catalytic hydrogenation and dehydrogenation of N-propylcarbazole, Int. J. Hydrog. Energy 48 (2023) 90–100.
[57] T. Zhu, M. Yang, X. Chen, Y. Dong, Z. Zhang, H. Cheng, A highly active bifunctional Ru–Pd catalyst for hydrogenation and dehydrogenation of liquid organic hydrogen carriers, J. Catal. 378 (2019) 382–391.
[58] F. Hess, B.M. Smarsly, H. Over, Catalytic stability studies employing dedicated model catalysts, Acc. Chem. Res. 53 (2020) 380–389.
[59] S. Lin, Q. Wang, M. Li, Z. Hao, Y. Pan, X. Han, X. Chang, S. Huang, Z. Li, X. Ma, Ni–Zn dual sites switch the CO_2 hydrogenation selectivity via tuning of the d-band center, ACS Catal. 12 (2022) 3346–3356.
[60] D.R. Aireddy, K. Ding, Heterolytic dissociation of H_2 in heterogeneous catalysis, ACS Catal. 12 (2022) 4707–4723.
[61] Y. Zhao, T. Wang, Y. Wang, R. Hao, H. Wang, Y. Han, Catalytic reduction of CO_2 to HCO_2^- by nanoscale nickel-based bimetallic alloy under atmospheric pressure, J. Ind. Eng. Chem. 77 (2019) 291–302.
[62] F. Sun, Y. An, L. Lei, F. Wu, J. Zhu, X. Zhang, Identification of the starting reaction position in the hydrogenation of (N-ethyl)carbazole over Raney-Ni, J. Energy Chem. 24 (2015) 219–224.